ANZIAM J. **62** (2020), 406–422
doi:10.1017/S1446181120000036

THE ALTERNATIVE KIRCHHOFF APPROXIMATION IN ELASTODYNAMICS WITH APPLICATIONS IN ULTRASONIC NONDESTRUCTIVE TESTING

L. J. FRADKIN[1], A. K. DJAKOU[2], C. PRIOR[3], M. DARMON[4], S. CHATILLON[4] and P.-F. CALMON[4]

(Received 12 June, 2019; accepted 14 January, 2020; first published online 23 April, 2020)

Abstract

The Kirchhoff approximation is widely used to describe the scatter of elastodynamic waves. It simulates the scattered field as the convolution of the free-space Green's tensor with the geometrical elastodynamics approximation to the total field on the scatterer surface and, therefore, cannot be used to describe nongeometrical phenomena, such as head waves. The aim of this paper is to demonstrate that an alternative approximation, the convolution of the far-field asymptotics of the Lamb's Green's tensor with incident surface tractions, has no such limitation. This is done by simulating the scatter of a critical Gaussian beam of transverse motions from an infinite plane. The results are of interest in ultrasonic nondestructive testing.

2010 *Mathematics subject classification*: primary 74H15; secondary 74H10, 74J05, 74J10, 74J15, 74J20, 74L99.

Keywords and phrases: nondestructive testing, ultrasound, high-frequency asymptotics, Lamb's Green's tensor, critical Gaussian beam.

1. Introduction

Nondestructive testing (NDT) is commonly used to assess size, location and orientation of flaws in industrial structures. Ultrasonic inspections offer the least expensive alternative. In the nuclear industry, it is a legal requirement that NDT inspectors carry out inspection qualification to demonstrate that safety critical defects can be detected. As part of inspection qualification, they routinely perform computer

[1]Sound Mathematics Ltd., Cambridge CB4 2AS, UK; e-mail: l.fradkin@soundmathematics.com.
[2]Sound Mathematics Ltd., Cambridge CB4 2AS, UK. Now at GEFCO, Courbevoie Cedex, France; e-mail: noelleaudrey@yahoo.fr.
[3]Sound Mathematics Ltd., Cambridge CB4 2AS, UK. Now at Department of Mathematical Sciences, Durham University, Durham, UK; e-mail: christopher.prior@durham.ac.uk.
[4]CEA, LIST, Department of Imaging and Simulation for NDT, F-91191 Gif-sur-Yvette, France; e-mail: Michel.DARMON@cea.fr, Sylvain.CHATILLON@cea.fr, Pierre.CALMON@cea.fr.

simulation of relevant configurations. If necessary this can be done with commercial finite-element packages, but, when the speed of simulation is of essence, whenever possible, inspectors use packages such as CIVA [10], which utilize approximate tools for simulating radiation, propagation and scattering of ultrasonic pulses in solids. One such tool is the elastodynamic Kirchhoff approximation (KA) [4, 13] that relies on the well-known free-space Green's tensor for a homogeneous and isotropic solid as well as the classical assumptions of geometrical elastodynamics (GE): these are satisfied by large scatterers with locally straight edges, when both the incident wave front and the scatterer surface are locally plane. The industrial ultrasonic probes operate at relatively high frequencies, so these assumptions usually hold.

The KA cannot be used to simulate nongeometric phenomena, such as head waves, which arise when the wave fronts or scatterers are curved or contain irregularities. One circumstance in which such waves make a significant contribution arises when the probing beam of T (transverse) motions is incident on the plane surface at the critical angle. Then the reflected T beam and head wave both propagate in the same direction and may experience destructive interference. The accompanying effects are beam shifting (the Goos–Hänchen effect) [12] and a Goodier–Bishop-type wave [14].

In order to overcome this drawback we propose to simulate nongeometric aspects of scatter using an alternative Kirchhoff approximation (AKA) that relies on (the high-frequency asymptotics) of the Lamb's Green's tensor instead of the free-space Green's tensor. The rationale behind the proposal is simple: the free-space Green's tensor does not contain any information on the boundary of the solid, while the Lamb's Green's tensor describes the field radiated by a point source situated on such boundary (provided its is planar) and using its far-field asymptotics can lead to a computer code that is still relatively fast. In this paper, we demonstrate capabilities of the AKA by simulating scatter of a critical Gaussian T beam by a planar scatterer. To be more precise, the incident beam is chosen to be generated by a CPS (complex point source), which in the paraxial approximation behaves as a Gaussian beam. Such beams serve as a good model of beams generated by industrial ultrasonic transducers, are easy to treat analytically and have intensity dropping at the beam boundary so fast that the geometrical elastodynamics does not apply.

The paper is organized as follows: the problem statement is offered in Section 2, followed by Section 3, where the incident CPS beam is described. The exact integral representation of the Lamb's Green's tensor as well as its high-frequency asymptotics are introduced in Section 4 and appendices. The validation of AKA is presented in Section 5, followed by a conclusion in Section 6.

2. Problem statement

We consider the displacement fields $\mathbf{U}\exp[-i(\omega t) - \mathbf{kx}]$ created in an homogeneous and isotropic solid half-space by a time-harmonic load, where i is the imaginary unit, $\mathbf{x}$ is a point in space, t denotes time, ω is the circular frequency, $\mathbf{k}$ is the wave vector with amplitude $k = \omega/c$ and c is the wave speed. For simplicity of presentation, in the

https://doi.org/10.1017/S1446181120000036 Published online by Cambridge University Press

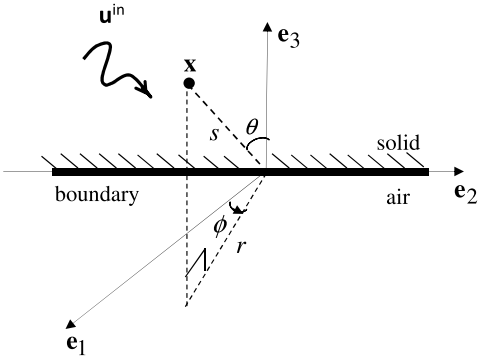

FIGURE 1. The scatterer Cartesian coordinate system and associated spherical polar coordinate system. Thick line denotes the boundary of a solid half-space.

rest of the paper, the exponential factor $\exp(-i\omega t)$ is omitted but implied everywhere. We use bold symbols to denote vectors and, when in regular font, the same symbols denote the corresponding amplitudes.

Let the scatterer be the planar boundary of this half-space. Let us introduce the scatterer Cartesian coordinate system $\{\mathbf{e}_1, \mathbf{e}_2, \mathbf{e}_3\}$ with $\mathbf{e}_3$, the inner normal to this boundary. The corresponding Cartesian coordinates of any vector $\mathbf{x}$ are (x_1, x_2, x_3) and associated spherical polar coordinates are (s, ϕ, θ) (see Figure 1). Throughout the paper, subscripts $k, l, m, n = 1, 2, 3$ refer to the respective coordinates in the appropriate Cartesian system. Other subscripts and superscripts are used to indicate the field type. In particular, descriptors *in*, *sc* and *tot* relate to the incident, scattered and total fields, respectively.

Inside the half-space, let the incident and total (and hence scattered) displacement vector fields, $\mathbf{u}(\mathbf{x}) = (u_m(\mathbf{x}))$, and the associated stress tensor fields, $\sigma(\mathbf{x}) = (\sigma_{\ell m}(\mathbf{x}))$, satisfy the reduced equations of motion of linear elasticity (see, for example, [8, § 5.1]),

$$\sigma_{\ell m,\ell} + \rho\omega^2 u_m = 0, \tag{2.1}$$

as well as Hooke's law [8, equation (A.5.13)]

$$\sigma_{\ell m} = \rho c_T^2 (u_{\ell,m} + u_{m,\ell}) + \rho c_L^2 (1 - 2\gamma^2)\delta_{\ell m} u_{n,n}], \tag{2.2}$$

where $\delta_{\ell m}$ is the Kronecker delta, the subscript k denotes the partial derivative with respect to x_k, ρ is the material density, c_L, c_T are the L (longitudinal) and T (transverse) speeds, respectively, $\gamma = c_T/c_L < 1$, and the summation convention implied. Also let the boundary be subjected to an integrable incident traction (see [8, equation (5.1.39)])

$$\mathbf{t}^{in} = \sigma^{in} \cdot \mathbf{e}_3 \tag{2.3}$$

and impose the stress-free boundary condition [8, equation (6.1.13)]

$$\sigma^{sc}_{\ell 3}(\mathbf{x})|_{x_3=0^+} = -t^{in}_{\ell}(\mathbf{x})|_{x_3=0^+}.$$

https://doi.org/10.1017/S1446181120000036 Published online by Cambridge University Press

In addition, let us assume the usual radiation condition (see [8, § 1.1.7]) that when k_T is complexified with a small complex part, all outgoing waves decay at infinity.

The above BVP (boundary value problem) can be formulated via Green's theorem [13, equation (5.57)] to represent the scattered field $\mathbf{u}^{sc}(\mathbf{x})$ as the convolution of the free-space Green's stress tensor of the third rank $\sigma^G(\mathbf{x})$ and (an unknown) surface displacement $\mathbf{u}^{tot}(\mathbf{x}') = \mathbf{u}^{in}(\mathbf{x}') + \mathbf{u}^{sc}(\mathbf{x}')$,

$$u_\ell^{sc}(\mathbf{x}) = -\int_{-\infty}^{\infty}\int_{-\infty}^{\infty} \sigma_{\ell 3k}^{G}(\mathbf{x}-\mathbf{x}')\, u_k^{tot}(\mathbf{x}')\, dx_1'\, dx_2' \tag{2.4}$$

with $\mathbf{x}' = (x_1', x_2', 0)$ an arbitrary surface point; and the stress tensor σ^G associated with the second-rank free-space Green's tensor $G_{\ell k}$ – the displacement due to $\delta_{\ell k}\delta(\mathbf{x}-\mathbf{x}')$, the delta function type point source at $\mathbf{x}'$. The standard KA utilizes this relationship and the assumption that on the shadow side of the boundary, $\mathbf{u}^{tot}(\mathbf{x}')$ is zero and, on the irradiated side, it is the sum of incident and reflected fields (see [13, § 6.6]).

Let us now introduce the Lamb's Green's tensor of the second rank $G^{\mathrm{Lamb}}(\mathbf{x})$ and the stress tensor of the third rank $\sigma^{\mathrm{Lamb}}(\mathbf{x})$, solutions of (2.1) supplied with the same radiation condition as above and the boundary condition

$$\sigma_{\ell 3k}^{\mathrm{Lamb}}(\mathbf{x})|_{x_3=0^+} = -\delta_{\ell k}\delta(\mathbf{x})|_{x_3=0^+}. \tag{2.5}$$

It is easy to check by substitution that the convolution

$$u_\ell^{sc}(\mathbf{x}) = \int_{-\infty}^{\infty}\int_{-\infty}^{\infty} G_{\ell k}^{\mathrm{Lamb}}(\mathbf{x}-\mathbf{x}')\, t_k^{in}(\mathbf{x}')\, dx_1'\, dx_2' \tag{2.6}$$

solves the same BVP as (2.4). In physical terms, (2.6) represents the Huygens principle: the displacement is the superposition of the displacements generated by the elementary point loads on the scatterer surface. Below we derive expressions for G^{Lamb} and construct the AKA by substituting into (2.6) the far-field asymptotics of this tensor.

3. Incident tractions

Let us assume that the incident field in (2.6) is due to a CPS.

3.1. Complex point source To introduce a CPS, we first consider an ordinary point source $U_0\,\delta(\mathbf{x}-\mathbf{a})$ at point $\mathbf{a}$. It radiates the outgoing spherical field $U_0\,G$, where the reduced free-space Green's tensor has components [3, equation (2.5.54)]

$$G_{\ell k} = \frac{1}{\rho c_T^2}[k_T^{-2}(I_T - I_L)_{,\ell k} + I_T\delta_{\ell k}], \quad I_\alpha = \frac{e^{ik_\alpha s_{in}}}{4\pi s_{in}} \tag{3.1}$$

with $s_{in} = \sqrt{(x_1-a_1)^2 + (x_2-a_2)^2 + (x_3-a_3)^2}$ and $\alpha = T$ or L.

Let us complexify the first coordinate of $\mathbf{a}$. This operation turns the spherical field into a beam, which propagates along the axis singled out by the complexification process [5]. Introducing the beam Cartesian coordinate systems $\{\bar{\mathbf{e}}_1, \bar{\mathbf{e}}_2, \bar{\mathbf{e}}_3\}$ shown

https://doi.org/10.1017/S1446181120000036 Published online by Cambridge University Press

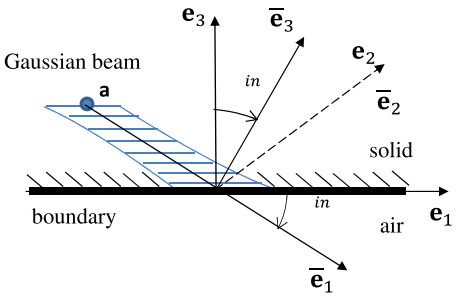

FIGURE 2. Scatterer/beam coordinate systems $\{\mathbf{e}_1, \mathbf{e}_2, \mathbf{e}_3\}/\{\bar{\mathbf{e}}_1, \bar{\mathbf{e}}_2, \bar{\mathbf{e}}_3\}$.

in Figure 2, this beam axis lies in the $(\bar{\mathbf{e}}_1, \bar{\mathbf{e}}_3)$ plane, the beam coordinates of the source $\mathbf{a}$ are $(-\bar{a}_1, 0, 0)$ and the beam coordinates of its complexified version $\mathbf{A}$ are $(-\bar{a}_1 + ia_R, 0, 0)$. Figure 2 introduces ϑ^{in}, the supplementary angle between $\mathbf{e}_1$ and the beam axis, and, below, we sometimes make use of its counterpart $\bar{\vartheta}^{in} = -\vartheta^{in}$. For a point load $\mathbf{f}\delta(\mathbf{x} - \mathbf{A})$, the resulting displacement is

$$\mathbf{U}_{CPS} = U_0 G(\mathbf{x}, \mathbf{A})\mathbf{f}. \tag{3.2}$$

Introducing the distance along the beam axis $\Delta\bar{x}_1 = \bar{x}_1 + \bar{a}_1$, in the paraxial approximation $\bar{x}_2^2 + \bar{x}_3^2 \ll (\Delta\bar{x}_1)^2$, the complexified distance between an arbitrary point $\mathbf{x}$ and the complexified source $\mathbf{A}$ can be approximated in the following manner:

$$\sqrt{(\Delta\bar{x}_1 - ia_R)^2 + \bar{x}_2^2 + \bar{x}_3^2} \approx \Delta\bar{x}_1 - ia_R + \frac{1}{2}\frac{\bar{x}_2^2 + \bar{x}_3^2}{\Delta\bar{x}_1 - ia_R}.$$

Therefore, on the surface of the scatterer, inside the beam, $\Delta\bar{x}_1$ can be treated as constant and

$$\bar{I}_\alpha \approx -\frac{i}{4\pi}\frac{w_0}{w(\bar{x}_1)} e^{k_\alpha\{a_R - (\bar{x}_2^2+\bar{x}_3^2)/2w^2\}} e^{ik_\alpha\{\Delta\bar{x}_1 + (\bar{x}_2^2+\bar{x}_3^2)/2\varrho\} - i\zeta},$$

demonstrating that in the paraxial approximation the CPS field behaves as a three-dimensional Gaussian beam [12] with $\sqrt{2w^2(\Delta\bar{x}_1)/k_\alpha}$ as the beam spot (the radius of the beam at a distance $\Delta\bar{x}_1$ from the waist), $\sqrt{2w^2(0)/k_\alpha}$ as the beam spot at the waist, a_R as the Rayleigh length (the distance along the propagation direction of the beam from its waist to where the beam spot increases by $\sqrt{2}$), $\varrho = \varrho(\Delta\bar{x}_1)$ as the radius of curvature of the beam wave front, and $\zeta = \zeta(\Delta\bar{x}_1)$ as the Gouy phase shift, where

$$\varrho = \Delta\bar{x}_1\Big[1 + \Big(\frac{a_R}{\Delta\bar{x}_1}\Big)^2\Big], \quad w^2 = a_R\Big[1 + \Big(\frac{\Delta\bar{x}_1}{a_R}\Big)^2\Big], \quad \zeta = \frac{1}{2}\tan^{-1}\frac{\Delta\bar{x}_1}{a_R}.$$

Here, $w = w(\Delta\bar{x}_1)$. It is reasonable to select the constant $U_0 = \exp(-k_\alpha a_R)$.

3.2. Surface tractions due to complex point source Let us now find the incident surface tractions $t_\ell^{in}(x_1', x_2', 0)$ generated by a CPS. Applying (2.2) to the complexified version of (3.1), the beam coordinates of the corresponding stress tensor become

$$\bar{\sigma}_{\ell mk}^G = \rho c_T^2[\bar{G}_{\ell k,m} + \bar{G}_{mk,\ell} + \gamma^{-2}(1 - 2\gamma^2)\bar{G}_{nk,n}\delta_{\ell m}]. \tag{3.3}$$

https://doi.org/10.1017/S1446181120000036 Published online by Cambridge University Press

Using beam coordinates $(\bar{x}_1, \bar{x}_2, \bar{x}_3)$ and their complexified version

$$\bar{X}_1 = \Delta\bar{x}_1 - ia_R, \quad \bar{X}_2 = \bar{x}_2, \quad \bar{X}_3 = \bar{x}_3,$$

the derivatives of I_T-terms and I_L-terms in (3.3) become

$$\begin{aligned}
\bar{I}_{\alpha,\ell} &= \frac{I_\alpha}{S_{in}^2}(ik_\alpha S_{in} - 1)\bar{X}_\ell,\\
\bar{I}_{\alpha,\ell m} &= \frac{I_\alpha}{S_{in}^4}[(3 - 3ik_\alpha S_{in} - k_\alpha^2 S_{in}^2)\bar{X}_\ell\bar{X}_m + S_{in}^2(ik_\alpha S_{in} - 1)\delta_{\ell m}],\\
\bar{I}_{\alpha,\ell mk} &= \frac{I_\alpha}{S_{in}^6}[(-15 + 15ik_\alpha S_{in} + 6k_\alpha^2 S_{in}^2 - ik_\alpha^3 S_{in}^3)\bar{X}_\ell\bar{X}_m\bar{X}_k\\
&\quad + S_{in}^2(3 - 3ik_\alpha S_{in} - k_\alpha^2 S_{in}^2)(\bar{X}_\ell\delta_{mk} + \bar{X}_m\delta_{\ell k} + \bar{X}_k\delta_{\ell m})].
\end{aligned}$$

Using (2.3), (3.2) and the beam coordinates of both the normal $\mathbf{n} = \mathbf{e}_3$ and the point load $\mathbf{f}$, at the surface point $\mathbf{x}'$, the components of the incident surface traction are

$$\bar{t}_\ell^{in} = \bar{\sigma}_{\ell mk}^G \bar{n}_m \bar{f}_k.$$

4. The Lamb's Green's tensor

The components of the Lamb's Green's tensor have no analytical expressions, but their Fourier transforms do. These are derived below.

4.1. The Lamb's Green's tensor in the Fourier space

We introduce the relevant Fourier transforms first. In an isotropic and homogeneous space, there is no difference between directions, but the plane boundary singles out the direction of its normal. For this reason, we utilize the double spatial transform defined for any integrable function $f(x_1, x_2)$ as

$$\tilde{f}(\xi_1, \xi_2) = \int_{-\infty}^{\infty}\int_{-\infty}^{\infty} f(x_1,\ x_2)e^{-ik_T(\xi_1 x_1 + \xi_2 x_2)}\, dx_1\, dx_2. \tag{4.1}$$

Its inverse is the usual spectrum of the outgoing waves

$$f(x_1, x_2) = \frac{k_T^2}{4\pi^2}\int_{-\infty}^{\infty}\int_{-\infty}^{\infty} \tilde{f}(\xi_1, \xi_2)e^{ik_T(\xi_1 x_1 + \xi_2 x_2)}\, d\xi_1\, d\xi_2. \tag{4.2}$$

Above, $\boldsymbol{\xi} = (\xi_1, \xi_2, \xi_3)$ are dimensionless wave vectors. Introducing $\xi_\perp = \sqrt{\xi_1^2 + \xi_2^2}$ and $\gamma_\alpha = c_T/c_\alpha$, their magnitudes are $\xi^\alpha = \gamma_\alpha$ and their third components are given by

$$\xi_3^\alpha = \sqrt{\gamma_\alpha^2 - \xi_\perp^2} \tag{4.3}$$

with the root chosen to be principal, so that the outgoing waves $\mathbf{u}\exp i(-\omega t + k_T\boldsymbol{\xi}\cdot\mathbf{x})$ decay at infinity and thus satisfy the radiation condition.

Applying (4.1) to (2.1), the double Fourier transforms of each column k of the Lamb's Green's tensor can be represented as a sum of TV (transverse vertical), TH (transverse horizontal) and L (longitudinal) components,

$$\widetilde{\mathbf{G}}_k^{\text{Lamb}}(\xi_1, \xi_2, x_3) = \widetilde{\mathbf{U}}_k^{TV} e^{ik_T\xi_3^T x_3} + \widetilde{\mathbf{U}}_k^{TH} e^{ik_T\xi_3^T x_3} + \widetilde{\mathbf{U}}_k^{L} e^{ik_T\xi_3^L x_3}. \tag{4.4}$$

https://doi.org/10.1017/S1446181120000036 Published online by Cambridge University Press

The amplitudes $\widetilde{\mathbf{U}}_\ell^\beta = \widetilde{\mathbf{U}}_\ell^\beta(\xi_1,\xi_2) = \widetilde{U}_\ell^\beta(\xi_1,\xi_2)\widetilde{\mathbf{d}}^\beta(\xi_1,\xi_2)$ can be found by applying (4.1) to (2.5) (see Appendix A).

4.2. The Lamb's Green's tensor in the physical space Using Appendix A and (4.2) in the physical space, the columns of the Lamb's Green's tensor can be represented as the double integrals

$$\mathbf{G}_k^{\mathrm{Lamb}}(\mathbf{x}-\mathbf{x}') = \frac{k_T^2}{4\pi^2}\iint\{\widetilde{\mathbf{U}}_k^T e^{ik_T\boldsymbol{\xi}^T\cdot(\mathbf{x}-\mathbf{x}')} + \widetilde{\mathbf{U}}_k^L e^{ik_T\boldsymbol{\xi}^L\cdot(\mathbf{x}-\mathbf{x}')}\}\,d\xi_1\,d\xi_2, \tag{4.5}$$

where $\widetilde{\mathbf{U}}_k^T = \widetilde{\mathbf{U}}_k^{TV} + \widetilde{\mathbf{U}}_k^{TH}$. It is convenient to introduce cylindrical coordinates $(\xi_\perp,\varphi)$, such that $\xi_1 = \xi_\perp\cos\varphi$, $\xi_2 = \xi_\perp\sin\varphi$, $x_1 - x_1' = r'\cos\phi'$, $x_2 - x_2' = r'\sin\phi'$ and express the TV components of the Lamb's Green's tensor as

$$G_{\ell k}^{\mathrm{Lamb}(TV)}(\mathbf{x}-\mathbf{x}') = \frac{ik_T}{2\pi\rho c_T^2}\int_0^\infty A_{\ell k}\,g_k^{(2)}\frac{\xi_\perp^2(1-2\xi_\perp^2)}{R(\xi_\perp^2)}e^{ik_T\xi_3^T x_3}\,d\xi_\perp. \tag{4.6}$$

Here, $g_1^{(2)} = \xi_3^T$, $g_2^{(2)} = \xi_3^T$, $g_3^{(2)} = -\xi_\perp$. Combining Euler's formula, the standard definition of the Bessel function $J_p(z)$ [1, equation (9.1.21)] as well as the identity $J_{-p}(z) = -J_p(z)$ with $p = 0^-$ treated as $p = 0^+$, the components of the symmetric matrix A are

$$A_{11} = \tfrac{1}{2}[J_0(k_T\xi_\perp r') - i\sin(2\phi')J_2(k_T\xi_\perp r')],$$
$$A_{12} = -i\cos(2\phi')J_2(k_T\xi_\perp r'),\quad A_{22} = \tfrac{1}{2}[J_0(k_T\xi_\perp r') + i\sin(2\phi')J_2(k_T\xi_\perp r')],$$
$$A_{13} = i\cos(\phi')J_1(k_T\xi_\perp r'),\quad A_{23} = i\sin(\phi')J_1(k_T\xi_\perp r'),\quad A_{33} = J_0(k_T\xi_\perp r').$$

Integrals (4.6) can be evaluated with a two-dimensional variable step version of the Simpson rule [6]. There is no need to derive similar results for TH and L components, because their stationary phase asymptotics give satisfactory results (see below).

4.3. Numerical evaluation of integral (2.6) It can be checked that at the Rayleigh distance a_R from the waist, the boundary value of the intensity of the Gaussian beam falls from its axial value by a factor of $\exp(-2)$. Therefore, choosing $a_1 = a_R$, a reasonable approximation to (4.5) can be achieved by reducing the integration domain to the footprint of the beam on the scattering surface (see Figure 2). This footprint is an ellipse with the axes $a_{\min} = 2\sqrt{a_R/k_\alpha}$ and $a_{\max} = 2\sqrt{a_R/k_\alpha}/\cos\vartheta^{in}$. Hence, its boundary can be described by the parametric equations

$$x_1' = a_{\max}\cos\varphi',\quad x_2' = a_{\min}\sin\varphi' = a_{\max}\cos\bar{\vartheta}^{in}\sin\varphi'.$$

We introduce the corresponding circular coordinates (a',φ')

$$x_1' = a'\cos\varphi',\quad x_2' = a'\cos\bar{\vartheta}^{in}\sin\varphi'.$$

The Jacobian of transformation from (x_1', x_2') coordinates to (a',φ') coordinates is $a'\cos\bar{\vartheta}^{in}$. It follows that (2.6) can be approximated using

$$u_\ell^{sc(\beta)}(\mathbf{x}) \simeq \cos\bar{\vartheta}^{in}$$
$$\times\int_0^{2\pi}\int_0^{a_{\max}} G_{\ell k}^{\mathrm{Lamb}(\beta)}(x_1 - a'\cos\varphi', x_2 - a'\cos\vartheta_{in}\sin\varphi', x_3)t_k{}^{in}(a',\phi')a'\,da'\,d\varphi'. \tag{4.7}$$

https://doi.org/10.1017/S1446181120000036 Published online by Cambridge University Press

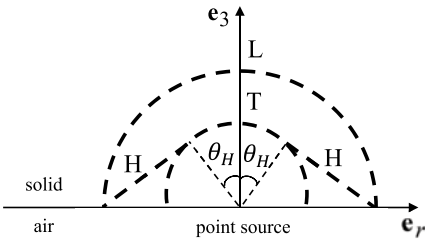

FIGURE 3. Wave fronts generated by a normal point load.

In order to evaluate this integral numerically, we employ a two-dimensional Simpson's scheme with the intervals $[0, a_{\max}]$ and $[0, 2\pi]$ divided, respectively, into N_f and M_f equal subintervals, and also specify the grid of evenly distributed observation points. Below we plot results in the x_1x_3-plane only, and N_o and M_o are the numbers of nodes in x_1- and x_3-directions, respectively. When dealing with the exact expression for the Lamb's Green's tensor, considerable reduction in runtime is achieved by specifying the footprint grid first and a convenient grid of observation points, afterwards.

5. The alternative Kirchhoff approximation and its validation

If the Lamb's Green's tensor in (4.7) is evaluated numerically, the resulting codes have long runtimes. Fortuitously, the ultrasonic inspections are normally conducted in the far field $|k_L x_3| \gg 1$, where x_3 is the vertical distance from the observation point to the scatterer. In this approximation, the double integrals in (4.5) contain a rapidly oscillating exponent and a slowly varying amplitude and, therefore, can be evaluated using the uniform stationary phase method [2]. The method describes asymptotic contributions of such critical points as stationary points of the phase and singularities of the amplitude, both in the geometrical regions in the scattered field where the critical points are isolated, and transition regions where some of them coalesce.

It is easy to check that in (4.5), the phases $k_\alpha \boldsymbol{\xi}^T \cdot (\mathbf{x} - \mathbf{x}')$ possess stationary points, and the amplitudes have poles as well as branch points $\xi_\perp = \pm\gamma$, where $\xi_3^L = 0$. These amplitude singularities give rise to the Rayleigh wave and head wave, respectively. Calculation of the Rayleigh wave is easy, and lies outside the scope of this paper. The simplest situation giving rise to a head wave is discussed in [7] and presented in Figure 3, where the fronts of transverse, longitudinal and head waves are designated by T, L and H, respectively. The T and L fronts are semi-spherical and the conical H front exists only for $\theta > \theta_H$.

To evaluate the contributions of the isolated stationary phase points, for each surface point $\mathbf{x}'$ let us choose the Cartesian coordinate system with the origin at this point. The associated cylindrical coordinates are (r', s', θ'), where

$$\Delta x_n' = x_n - x_n', \; n = 1, 2, \quad r' = \sqrt{\Delta x_1'^2 + \Delta x_2'^2}, \quad s' = \sqrt{r'^2 + x_3^2}, \quad \sin\theta' = r'/s'$$

https://doi.org/10.1017/S1446181120000036 Published online by Cambridge University Press

(see Figure 1). In these coordinates, the phase functions in (4.5) are

$$f^{\alpha}(\xi_1,\xi_2)=\xi_1\Delta x_1'+\xi_2\Delta x_2'+\sqrt{\gamma_\alpha^2-\xi_\perp^2}\,x_3.$$

Their stationary points and associated values are, respectively,

$$(\xi_1^{\alpha(GE)},\xi_2^{\alpha(GE)})=(\gamma_\alpha\Delta x_1'/s',\gamma_\alpha\Delta x_2'/s'),\quad f^{\alpha}(\xi_1^{\alpha(GE)},\xi_2^{\alpha(GE)})=s',\quad \xi_\perp^{\alpha(GE)}=\gamma_\alpha\sin\theta'.$$

The eigenvalues of each Hessian $(f^{\alpha})''(\xi_1^{\alpha(GE)},\xi_2^{\alpha(GE)})$ are positive. The above considerations allow us to produce an asymptotic description of TV, TH and L waves generated by each Huygens source (see Appendix B). The superscript GE emphasizes that the same description can be obtained using the geometrical elastodynamics.

The asymptotic contributions of branch points $\xi_\perp=\pm\gamma$, where $\xi_3^L=0$ (see (4.3)), are also well known [3]. However, in industrial steels these asymptotics do not work well [9]. For this reason, we do not use them and advocate the AKA instead, that is, substitute into (2.6) the amplitudes $G_{\ell k}^{\mathrm{Lamb}(\beta,GE)}$ (for $\beta=TV,TH$ or L) of the semi-spherical waves from Appendix B. Note that the components $G_{\ell k}^{\mathrm{Lamb}(TV,GE)}$ possess branch points at $\sin\theta'=\pm\gamma$ and, therefore, retain information about the branch points in the Fourier space.

The AKA has been tested by simulating scatter of Gaussian beams oscillating at $f=\omega/2\pi=5$ MHz, a typical frequency of industrial transducers, from the surface of a block of stainless steel with $c_L=5890\ \mathrm{ms}^{-1}$, $c_T=3210\ \mathrm{ms}^{-1}$ and $\rho=8050\ \mathrm{kg\ m}^{-3}$. The corresponding critical incident angle is $\vartheta^{in}=\cos^{-1}\gamma\approx-57°(\theta^{in}\approx33°)$.

Figures 4(c) and 4(d) simulate reflection of the subcritical T Gaussian beam. For comparison, reflection of the L beam is shown in Figures 4(a) and 4(b). As expected, the L beams have a wavelength twice as large and display larger footprints.

In both $L-L$ or $T-T$ cases, the reflection takes place according to Snell's law for elastic waves [8, equation (6.1.33)]. By contrast, Figure 4(e) shows the full scatter of the T beam into a weaker upper beam (reflected according to Snell's law) and a stronger lower beam (propagating at the critical angle). In principle, beam splitting could be due to a variation in the incidence angle over the footprint, but inspection of the incident beams in Figure 4 shows no comparable variation. We conclude that the lower beam is formed by the head wave. This conclusion is supported further by the fact that the beam appears or disappears depending on whether, when imaginary, the radical $\sqrt{\gamma^2-\sin^2\theta'}$ is supplied with the + or − sign; such behaviour is typical to branch point contributions [6]. Figures 4(f) and 4(g) simulate scatter of the critical Gaussian T beam. They demonstrate a small Goos–Hänchen shift to the right: the reflected T wave and head wave both propagate at the same angle, and their interference breaks the incident/reflected beam symmetry.

Let us now compare KA and AKA. Figures 5(a) and 5(b) demonstrate that the two approximations produce similar scattered L beams—the fact that the KA beam is somewhat stronger might be due to the fact that KA does not allow for the head wave and the head wave energy must be distributed between T and L modes. For the same reason, when the incidence is subcritical, the KA T beam is stronger than the AKA

https://doi.org/10.1017/S1446181120000036 Published online by Cambridge University Press

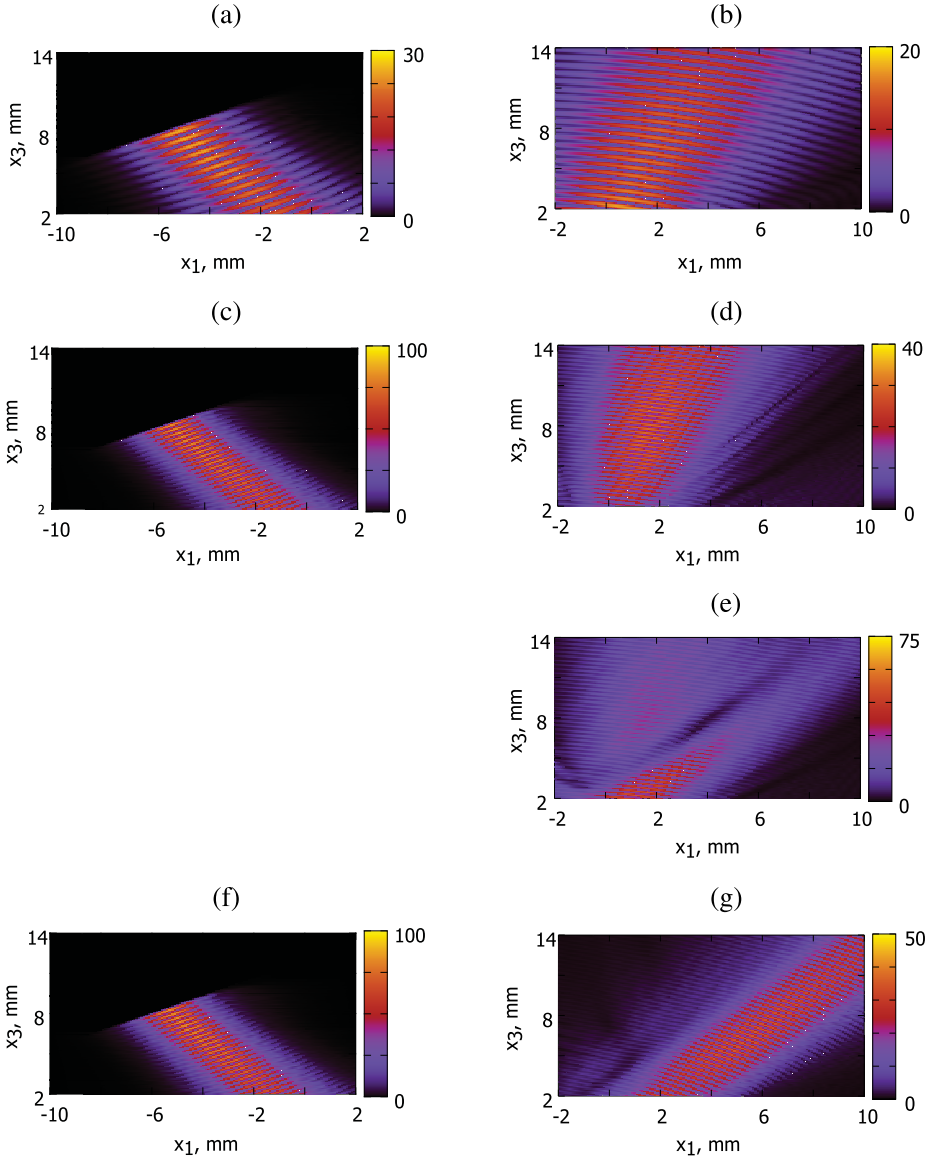

FIGURE 4. Simulation of scatter of Gaussian beams using AKA. The scalar displacement amplitude in the beam **u** is traditionally defined as $|\mathrm{Re}\sqrt{u_1^2+u_2^2+u_3^2}|$. The colour bar represents displacement amplitudes in pm.
$\vartheta_L^{in} = -75°$: (a) incident L beam, (b) reflected L beam;
$\vartheta_T^{in} = -75°$: (c) incident T beam, (d) reflected T beam, (e) reflected T beam and head wave beam;
$\vartheta_T^{in} = -\vartheta_H$: (f) incident T beam, (g) scattered T beam.
$N_o = 120, M_o = 120, N_f = 24, M_f = 40$.

https://doi.org/10.1017/S1446181120000036 Published online by Cambridge University Press

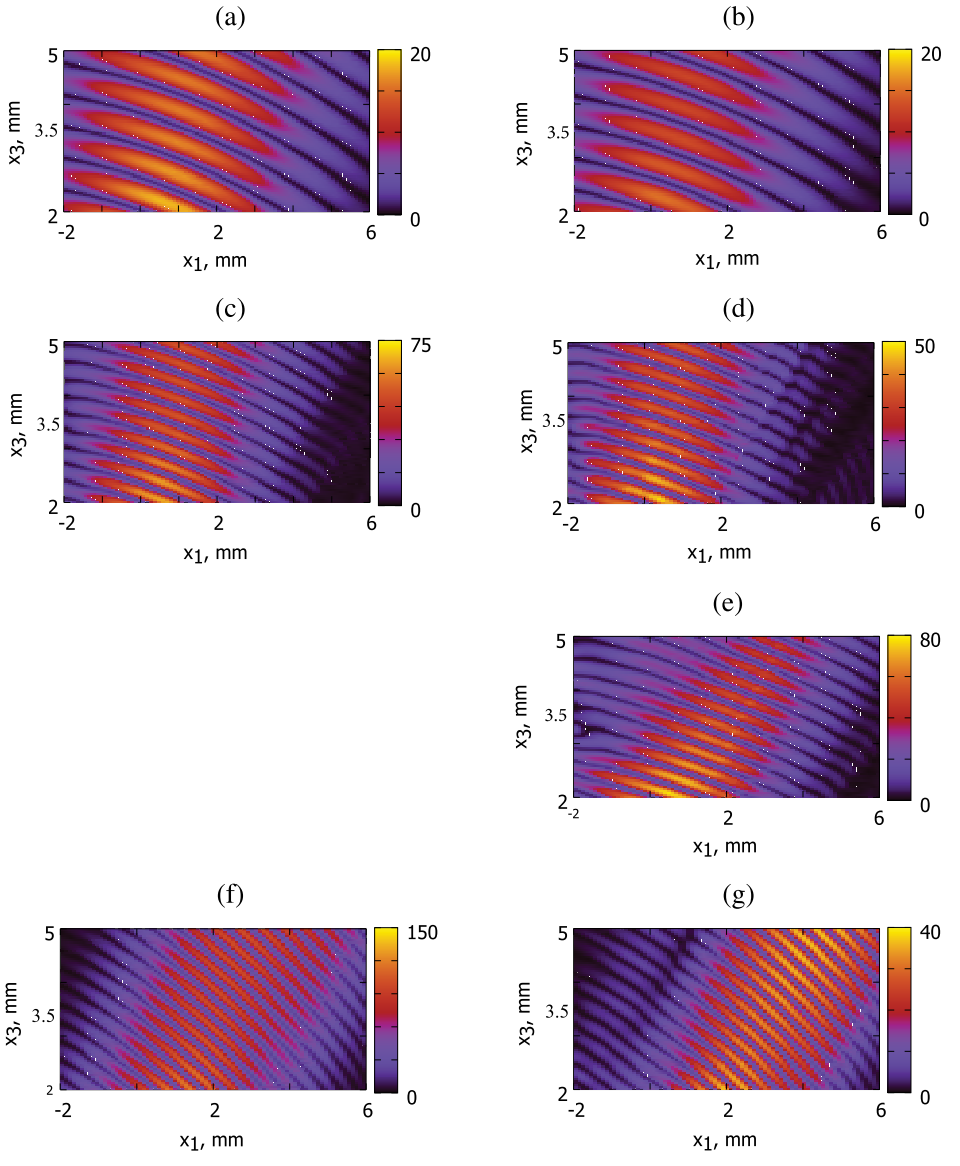

FIGURE 5. Comparison of KA and AKA of scattered Gaussian beams.
$\vartheta_L^{in} = -75°$, reflected L beam simulated using (a) KA, (b) AKA;
$\vartheta_T^{in} = -75°$, reflected T beam simulated using (c) KA, (d) AKA; reflected T beam and head wave beam simulated using (e) AKA;
$\vartheta_T^{in} = -\vartheta_H$, scattered T beam simulated using (f) KA, (g) AKA.
$N_f = 24, M_f = 40, N_o = 80, M_o = 80$. The colour bar is same as in Figure 4.

https://doi.org/10.1017/S1446181120000036 Published online by Cambridge University Press

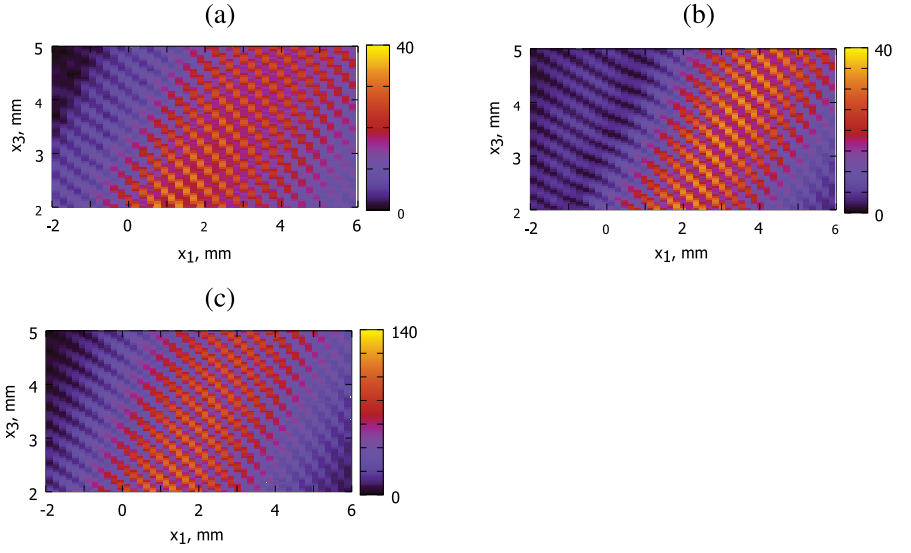

FIGURE 6. Comparison of TV components of scattered critical Gaussian beam simulated using (2.6) and (a) Section 4.2 ($N_f = 36, M_f = 40$), (b) AKA and (c) KA ($N_f = 36, M_f = 80$ for both). $N_o = 80, M_o = 40$. The colour bar is same as in Figure 4.

T beam (see Figures 5(c) and 5(d); cf. Figure 5(e)). At the critical incidence, KA produces a much stronger T beam than AKA and no Goos–Hänchen shift.

Finally, let us compare both AKA and KA to the exact numerical solution based on (4.7). Figure 6 shows that when the incident Gaussian T beam is critical, unlike KA and AKA, it produces reasonable results; it reproduces the footprint, angle of scatter and even the scattered intensity. Note that using an Intel (R) Core (TM) i3-3227U processor CPU @1.90 GHz, Figures 6(a) and 6(b) have been produced in 11 h and 4 min, respectively.

6. Conclusions

We have shown that while the KA is incapable of simulating head waves, the AKA simulates the effect similarly to the exact numerical solution, reproducing a small lateral Goos–Hänchen shift and—more importantly—the correct amplitude of the scattered critical Gaussian beam. The result is not obvious, because the asymptotic expressions of the Lamb's Green's tensor utilized in the AKA describe only the semi-spherical L and T waves generated by each Huygens source and not the associated head waves. On the other hand, the amplitudes of the T waves contain the square roots, retaining information about the square roots in their Fourier transforms, and it is these roots (more precisely, the fact that the integrands used in the AKA are double-valued functions) that give rise to the head waves. The findings are of interest in NDT applications.

https://doi.org/10.1017/S1446181120000036 Published online by Cambridge University Press

Appendix A

The Lamb's Green's tensor in Fourier space

Each component $G^{\mathrm{Lamb}}_{\ell k} = G^{\mathrm{Lamb}}_{\ell k}(x_1, x_2, x_3)$ of the Lamb's Green's tensor represents the ℓth component of the displacement $\mathbf{G}^{\mathrm{Lamb}}_k = \mathbf{G}^{\mathrm{Lamb}}_k(x_1, x_2, x_3)$, which is due to a unit traction acting in the direction $\mathbf{e}_k$. Therefore, the original problem can be decomposed into three, two—with the tangential unit traction acting in the direction $\mathbf{e}_1$ and $\mathbf{e}_2$ and one—with the traction acting normally to the surface. In order to find the Lamb's Green's tensor, we first rewrite equation (2.1) as

$$L_{m\ell} G^{\mathrm{Lamb}}_{\ell k} + \rho\omega^2 G^{\mathrm{Lamb}}_{mk} = 0, \tag{A.1}$$

where $L_{m\ell} = L_{m\ell}(\partial_1, \partial_2, \partial_3)$ are components of the operator matrix

$$L = \rho c_L^2 \begin{bmatrix} (1-\gamma^2)\partial_1^2 + \gamma^2\nabla^2 & (1-\gamma^2)\partial_1\partial_2 & (1-\gamma^2)\partial_1\partial_3 \\ (1-\gamma^2)\partial_1\partial_2 & (1-\gamma^2)\partial_2^2 + \gamma^2\nabla^2 & (1-\gamma^2)\partial_2\partial_3 \\ (1-\gamma^2)\partial_1\partial_3 & (1-\gamma^2)\partial_2\partial_3 & (1-\gamma^2)\partial_3^2 + \gamma^2\nabla^2 \end{bmatrix},$$

with ∂_ℓ as the partial derivative with respect to x_ℓ, and $\nabla^2 = \partial_1^2 + \partial_2^2 + \partial_3^2$. Applying to (A.1) the double Fourier transform (4.1), we obtain the system of ordinary differential equations

$$\widetilde{L}_{m\ell}(\xi_1, \xi_2, \partial_3)\widetilde{G}^{\mathrm{Lamb}}_{\ell k}(\xi_1, \xi_2, x_3) + \rho\omega^2 \widetilde{G}^{\mathrm{Lamb}}_{mk}(\xi_1, \xi_2, x_3) = 0. \tag{A.2}$$

We seek the outgoing solutions of this system in the form

$$\widetilde{\mathbf{G}}^{\beta\,(\mathrm{Lamb})}_k(\xi_1, \xi_2, x_3) = \widetilde{\mathbf{U}}^\beta_k(\xi_1, \xi_2) e^{ik_T\xi_3 x_3} = \widetilde{U}^\beta_k(\xi_1, \xi_2)\,\widetilde{\mathbf{d}}^\beta(\xi_1, \xi_2) e^{ik_T\xi_3 x_3}. \tag{A.3}$$

Substituting (A.3) into (A.2),

$$\widetilde{L}(\boldsymbol{\xi})\widetilde{\mathbf{U}}^\beta_k(\xi_1, \xi_2) = -\rho\omega^2 \widetilde{\mathbf{U}}^\beta_k(\xi_1, \xi_2), \tag{A.4}$$

where the operator $\widetilde{L} = \widetilde{L}(\boldsymbol{\xi})$ has components

$$\widetilde{L}_{m\ell} = -\rho\omega^2[(\gamma^{-2} - 1)\xi_m\xi_\ell + \xi^2\delta_{m\ell}]. \tag{A.5}$$

Equation (A.4) can be embedded into the so-called Kelvin–Cristoffel equation

$$\widetilde{L}\widetilde{\mathbf{d}}^\beta = -\rho\omega^2\nu_\beta\widetilde{\mathbf{d}}^\beta,$$

which possesses a nonzero solution only if

$$|\widetilde{L} + \rho\omega^2\nu I| = -\rho\omega^2(\xi^2 - \nu)^2(\gamma^{-2}\xi^2 - \nu) = 0,$$

where I is the unit matrix. It follows that the operator $\widetilde{L}$ has a double eigenvalue $\nu_T = \nu_{TV} = \nu_{TH} = \xi^2$ and a simple eigenvalue $\nu_L = \gamma^{-2}\xi^2$ with the corresponding eigenvectors $\widetilde{\mathbf{d}}^\beta = \widetilde{\mathbf{d}}^\beta(\xi_1, \xi_2)$ given by

$$\widetilde{\mathbf{d}}^{TV} = \begin{cases} \dfrac{1}{\xi_T\xi_\perp}\begin{pmatrix} \xi_1\xi_3^T \\ \xi_2\xi_3^T \\ -\xi_\perp^2 \end{pmatrix} & \\ \mathbf{e}_1 & \text{if } \xi_\perp = 0, \end{cases} \quad , \quad \widetilde{\mathbf{d}}^{TH} = \begin{cases} \dfrac{1}{\xi_\perp}\begin{pmatrix} \xi_2 \\ -\xi_1 \\ 0 \end{pmatrix} & \text{if } \xi_\perp \neq 0, \\ \mathbf{e}_2 & \text{if } \xi_\perp = 0, \end{cases} \quad \widetilde{\mathbf{d}}^L = \frac{1}{\xi_L}\begin{pmatrix} \xi_1 \\ \xi_2 \\ \xi_3^L \end{pmatrix}. \tag{A.6}$$

https://doi.org/10.1017/S1446181120000036 Published online by Cambridge University Press

As usual, there is arbitrariness in choosing eigenvectors corresponding to a double eigenvalue. The choice made in (A.6) ensures that $\lim_{\xi_\perp\to 0}(\xi_1/\xi_\perp) = 1$ and $\lim_{\xi_\perp\to 0}(\xi_2/\xi_\perp) = 0$. The eigenvectors in (A.6) become solutions of (A.5) when $\nu_\beta = 1$, that is, when $|k_T\boldsymbol{\xi}^\beta| = k_\beta$.

The unknown amplitudes $\widetilde{U}_k^\beta = \widetilde{U}_k^\beta(\xi_1, \xi_2)$ can be found from the boundary condition (2.5) rewritten as

$$B_{mk}\mathbf{G}_k^{\mathrm{Lamb}}|_{x_3=0^+} = -\delta_{mk}\delta(\mathbf{x})|_{x_3=0^+} \tag{A.7}$$

with $B_{mk} = B_{mk}(\partial_1, \partial_2, \partial_3)$ as elements of the operator matrix

$$B = \rho c_L^2 \begin{pmatrix} \gamma^2\partial_3 & 0 & \gamma^2\partial_1 \\ 0 & \gamma^2\partial_3 & \gamma^2\partial_2 \\ (1-2\gamma^2)\partial_1 & (1-2\gamma^2)\partial_2 & \partial_3 \end{pmatrix}.$$

The double Fourier transform of (A.7) is

$$\widetilde{B}\widetilde{\mathbf{G}}_k^{\mathrm{Lamb}}|_{x_3=0^+} = -\mathbf{e}_k \tag{A.8}$$

with the operator matrix $\widetilde{B} = \widetilde{B}(\xi_1, \xi_2, \partial_3)$ given by

$$\widetilde{B}(\xi_1, \xi_2, \partial_3) = \rho c_L^2 \begin{pmatrix} \gamma^2\partial_3 & 0 & \gamma^2 ik_T\xi_1 \\ 0 & \gamma^2\partial_3 & \gamma^2 ik_T\xi_2 \\ (1-2\gamma^2)ik_T\xi_1 & (1-2\gamma^2)ik_T\xi_2 & \partial_3 \end{pmatrix}.$$

Combining (A.3), (A.6) and (A.8) produces the linear algebraic system

$$\mathrm{A}\widetilde{\mathbf{U}}_k = \mathbf{c}_k, \tag{A.9}$$

where we use the notation

$$\mathrm{A} = \begin{cases} \begin{pmatrix} \xi_1(1-2\xi_\perp^2) & \xi_2\xi_3^T & 2\gamma^{-1}\xi_\perp\xi_1\xi_3^L \\ \xi_2(1-2\xi_\perp^2) & -\xi_1\xi_3^T & 2\gamma^{-1}\xi_\perp\xi_2\xi_3^L \\ -2\xi_3^T\xi_\perp^2 & 0 & \gamma^{-1}\xi_\perp(1-2\xi_\perp^2) \end{pmatrix} & \text{if } \xi_\perp \neq 0, \\ \begin{pmatrix} 1 & 0 & 0 \\ 0 & 1 & 0 \\ 0 & 0 & \gamma^{-1} \end{pmatrix} & \text{if } \xi_\perp = 0, \end{cases}$$

$$\widetilde{\mathbf{U}}_k(\xi_1, \xi_2) = \begin{pmatrix} \widetilde{U}_k^{TV} \\ \widetilde{U}_k^{TH} \\ \widetilde{U}_k^{L} \end{pmatrix}, \quad \mathbf{c}_k = \frac{i\xi_\perp}{k_T\rho c_T^2}\mathbf{e}_k.$$

For $\xi_\perp \neq 0$, $|\mathrm{A}| = -\gamma^{-1}\xi_\perp^3\xi_3^T R(\xi_\perp^2)$ with the Rayleigh function

$$R(\xi_\perp^2) = 4\xi_\perp^2\xi_3^T\xi_3^L + [1-2\xi_\perp^2]^2. \tag{A.10}$$

https://doi.org/10.1017/S1446181120000036 Published online by Cambridge University Press

Solving (A.9), the components of the vectors $\widetilde{\mathbf{U}}_k$ are

$$\begin{cases} \widetilde{U}_1^{TV} = \dfrac{i}{k_T\rho c_T^2}\dfrac{\xi_1(1-2\xi_\perp^2)}{\xi_\perp R(\xi_\perp^2)}, \quad \widetilde{U}_1^{TH} = \dfrac{i}{k_T\rho c_T^2}\dfrac{\xi_2}{\xi_\perp\xi_3^T} & \text{if } \xi_\perp \neq 0, \\ \widetilde{U}_1^{TV} = \dfrac{i}{k_T\rho c_T^2}, \quad \widetilde{U}_1^{TH} = 0 & \text{if } \xi_\perp = 0, \end{cases}$$

$$\widetilde{U}_1^{L} = \frac{2i}{k_L\rho c_L^2}\frac{\xi_1\xi_3^T}{R(\xi_\perp^2)},$$

$$\begin{cases} \widetilde{U}_2^{TV} = \dfrac{i}{k_T\rho c_T^2}\dfrac{\xi_2(1-2\xi_\perp^2)}{\xi_\perp R(\xi_\perp^2)}, \quad \widetilde{U}_2^{TH}(\xi_1,\xi_2) = -\dfrac{i}{k_T\rho c_T^2}\dfrac{\xi_1}{\xi_\perp\xi_3^T} & \text{if } \xi_\perp \neq 0, \\ \widetilde{U}_2^{TV} = 0, \quad \widetilde{U}_2^{TH} = \dfrac{i}{k_T\rho c_T^2} & \text{if } \xi_\perp = 0, \end{cases}$$

$$\widetilde{U}_2^{L} = \frac{2i}{k_L\rho c_L^2}\frac{\xi_2\xi_3^T}{R(\xi_\perp^2)},$$

$$\widetilde{U}_3^{TV} = -\frac{2i}{k_T\rho c_T^2}\frac{\xi_\perp\xi_3^L}{R(\xi_\perp^2)}, \quad \widetilde{U}_3^{TH} = 0, \quad \widetilde{U}_3^{L} = \frac{i}{k_L\rho c_L^2}\frac{1-2\xi_\perp^2}{R(\xi_\perp^2)}.$$

Each column of the Lamb's Green's tensor can be represented as a sum (4.4). Similar results have been obtained earlier for a linear source [11].

Appendix B

Stationary phase asymptotics of the Lamb's Green's tensor

Let us associate with each Huygens source $\mathbf{x}'$ a Cartesian coordinate system $\{\mathbf{e}_1', \mathbf{e}_2', \mathbf{e}_3\}$, with the origin at this source, and let all such systems be oriented in the same way as the scatterer coordinate system $\{\mathbf{e}_1, \mathbf{e}_2, \mathbf{e}_3\}$. Then all vectors have the same components in all of them. Evaluating the stationary phase asymptotics of (4.5), for each Huygens source the unit displacement vectors (A.6) and the Rayleigh functions (A.10) become, respectively,

$$\mathbf{d}^{TV}(\mathbf{x}-\mathbf{x}') = \begin{cases} \cos\theta'\,(\cos\phi'\,\mathbf{e}_1 + \sin\phi'\,\mathbf{e}_2) - \sin\theta'\,\mathbf{e}_3 & \text{if } r' \neq 0, \\ \mathbf{e}_1 & \text{if } r' = 0, \end{cases}$$

$$\mathbf{d}^{TH}(\mathbf{x}-\mathbf{x}') = \begin{cases} \sin\phi'\,\mathbf{e}_1 - \cos\phi'\,\mathbf{e}_2 & \text{if } r' \neq 0, \\ \mathbf{e}_2 & \text{if } r' = 0, \end{cases}$$

$$\mathbf{d}^{L}(\mathbf{x}-\mathbf{x}') = \sin\theta'\,(\cos\phi'\,\mathbf{e}_1 + \sin\phi'\,\mathbf{e}_2) + \cos\theta'\,\mathbf{e}_3,$$

and

$$R^T(\sin^2\theta') = 4\sin^2\theta'\cos\theta'\sqrt{\gamma^2 - \sin^2\theta'} + (1-2\sin^2\theta')^2,$$

$$R^L(\sin^2\theta') = 4\gamma^3\sin^2\theta'\cos\theta'\sqrt{1-\gamma^2\sin^2\theta'} + (1-2\gamma^2\sin^2\theta')^2,$$

https://doi.org/10.1017/S1446181120000036 Published online by Cambridge University Press

where ϕ' and θ' are specific to the source. Similar to Appendix A, the formal rule applied above is

$$\lim_{(x_1,x_2)\to(x_1',x_2')}(x_1-x_1')/r'=1 \quad \text{and} \quad \lim_{(x_1,x_2)\to(x_1',x_2')}(x_2-x_2')/r'=0.$$

The stationary phase contributions to the ℓ components of $\mathbf{G}_k^{\mathrm{Lamb}(GE)}=\mathbf{G}_k^{\mathrm{Lamb}(GE)}(\mathbf{x}-\mathbf{x}')$ become

$$G_{\ell 1}^{\mathrm{Lamb}(TV,GE)}=\begin{cases}-\dfrac{\cos\phi'}{2\pi\rho c_T^2}\,\dfrac{\cos\theta'(1-2\sin^2\theta')}{R^T(\sin^2\theta')}\,\dfrac{e^{ik_Ts'}}{s'}\,d_\ell^{TV} & \text{if } r'\neq 0,\\ -\dfrac{1}{2\pi\rho c_T^2}\,\dfrac{e^{ik_Ts'}}{s'}\,\delta_{\ell 1} & \text{if } r'=0,\end{cases}$$

$$G_{\ell 1}^{\mathrm{Lamb}(TH,GE)}=\begin{cases}-\dfrac{\sin\phi'}{2\pi\rho c_T^2}\,\dfrac{e^{ik_Ts'}}{s'}\,d_\ell^{TH} & \text{if } r'\neq 0,\\ 0 & \text{if } r'=0,\end{cases}$$

$$G_{\ell 1}^{\mathrm{Lamb}(L,GE)}=-\frac{\cos\phi'}{2\pi\rho c_L^2}\,\frac{\sin 2\theta'\sqrt{1-\gamma^2\sin^2\theta'}}{R^L(\sin^2\theta')}\,\frac{e^{ik_Ls'}}{s'}\,d_\ell^L,$$

$$G_{\ell 2}^{\mathrm{Lamb}(TV,GE)}=\begin{cases}-\dfrac{\sin\phi'}{2\pi\rho c_T^2}\,\dfrac{\cos\theta'(1-2\sin^2\theta')}{R^T(\sin^2\theta')}\,\dfrac{e^{ik_Ts'}}{s'}\,d_\ell^{TV} & \text{if } r'\neq 0,\\ 0 & \text{if } r'=0,\end{cases}$$

$$G_{\ell 2}^{\mathrm{Lamb}(TH,GE)}=\begin{cases}\dfrac{\cos\phi'}{2\pi\rho c_T^2}\,\dfrac{e^{ik_Ts'}}{s'}\,d_\ell^{TH} & \text{if } r'\neq 0,\\ -\dfrac{1}{2\pi\rho c_T^2}\,\dfrac{e^{ik_Ts'}}{s'}\,\delta_{\ell 2} & \text{if } r'=0,\end{cases}$$

$$G_{\ell 2}^{\mathrm{Lamb}(L,GE)}=-\frac{\sin\phi'}{2\pi\rho c_L^2}\,\frac{\sin 2\theta'\sqrt{1-\gamma^2\sin^2\theta'}}{R^L(\sin^2\theta')}\,\frac{e^{ik_Ls'}}{s'}\,d_\ell^L,$$

$$G_{\ell 3}^{\mathrm{Lamb}(TV,GE)}=\frac{1}{2\pi\rho c_T^2}\,\frac{\sin 2\theta'\sqrt{\gamma^2-\sin^2\theta'}}{R^T(\sin^2\theta')}\,\frac{e^{ik_Ts'}}{s'}\,d_\ell^{TV},$$

$$G_{\ell 3}^{\mathrm{Lamb}(L,GE)}=-\frac{1}{2\pi\rho c_L^2}\,\frac{\cos\theta'\,(1-2\gamma^2\sin^2\theta')}{R^L(\sin^2\theta')}\,\frac{e^{ik_Ls'}}{s'}\,d_\ell^L.$$

Acknowledgements

This work has been carried out within the framework of the CIVAMONT 2020 collaborative project. We thank Mr Flavien Deniaux for his contribution.

https://doi.org/10.1017/S1446181120000036 Published online by Cambridge University Press

References

[1] M. Abramowitz and I. A. Stegun, *Handbook of mathematical functions with formulas, graphs, and mathematical tables*. 10th edn (US Government Printing Office, Washington, DC, 1972).

[2] V. A. Borovikov, *Uniform stationary phase method* (IEE, London, 1994).

[3] V. Červenỳ, *Seismic ray theory* (Cambridge University Press, Cambridge, 2001).

[4] M. Darmon, N. Leymarie, S. Chatillon and S. Mahaut, "Modelling of scattering of ultrasounds by flaws for NDT", in: *Ultrasonic wave propagation in non homogeneous media, Volume 128 of Springer Proc. Phys.* (Springer, Berlin–Heidelberg, 2009) 61–71; doi:10.1007/978-3-540-89105-5_6.

[5] G. Deschamps, "Gaussian beam as a bundle of complex rays", *Electron. Lett.* **7** (1971) 684–685; doi:10.1049/el:19710467.

[6] L. Fradkin, M. Darmon, S. Chatilion and P. Calmon, "A semi-numerical model for near-critical angle scattering", *J. Acoust. Soc. Am.* **139** (2016) 141–150; doi:10.1121/1.4939494.

[7] L. J. Fradkin and A. P. Kiselev, "The two-component representation of time-harmonic elastic body waves in the high- and intermediate-frequency regimes", *J. Acoust. Soc. Am.* **101** (1997) 52–65; doi:10.1121/1.417970.

[8] K. F. Graft, *Wave motion in elastic solids* (Dover, New York, 1975).

[9] D. Gridin, "A fast method for simulating the propagation of pulses radiated by a rectangular normal transducer into an elastic half-space", *J. Acoust. Soc. Am.* **104** (1998) 3199–3211; doi:10.1121/1.423960.

[10] G. Huet, M. Darmon, A. Lhemery and S. Mahaut, "Modeling of corner echo ultrasonic inspection with bulk and creeping waves", in: *Ultrasonic wave propagation in non homogeneous media, Volume 128 of Springer Proc. Phys.* (Springer, Berlin, Heidelberg, 2009) 217–226; doi:10.1007/978-3-540-89105-5_19.

[11] G. F. Miller and H. Pursey, "The field and radiation impedance of mechanical radiators on the free surface of a semi-infinite isotropic solid", *Proc. R. Soc.* **223** (1954) 521–541; doi:10.1098/rspa.1954.0134.

[12] J. Pott and J. G. Harris, "Scattering of an acoustic Gaussian beam from a fluid–solid interface", *J. Acoust. Soc. Am.* **76** (1984) 1829–1838; doi:10.1121/1.391483.

[13] L. W. Schmerr, *Fundamentals of ultrasonic non-destructive evaluation: a modeling approach* (Plenum Press, New York, 1998).

[14] V. Zernov, L. Fradkin, A. Gautesen, M. Darmon and P. Calmon, "Wedge diffraction of a critically incident Gaussian beam", *Wave Motion* **50** (2013) 708–722; doi:10.1016/j.wavemoti.2013.01.004.